3.3 In-Plane Tensorial Stress Field Determination: CGS and Photoelasticity

3.3.1 Experimental Verification Test Problem

The experimental verification test specimen is a 12.7 mm × 12.7 mm square plate with thickness $h = 1.0$ mm and with a 60^o V-notch cut out of the side of the plate, just as it is for the experimental verification Chapter 2, shown in Figure 2.3. The depth of the V-notch, d, is 6.35 mm, and the V-notch opening width, w, is 7.34 mm. The plate is polycarbonate, which is a thermoplastic polymer that is highly photoelastic, with absolute photoelastic constants $A = -2.45 * 10^{-11}$ m^2/N and $B = -9.38*10^{-11}$ m^2/N, and therefore the relative photoelastic constant is $c_o = A - B = 6.93*10^{-11}$ m^2/N (Shimizu et al., 1998). This plastic has a Young's modulus of $E = 2.3$ GPa, Poisson's ratio of $\nu = 0.36$, and refractive index of $n_o = 1.586$. The photoelasticity-related constants used in calculating φ_{sum} and φ_{diff} are therefore $C = 1.51 \times 10^{-10}$ m^2/N and $g = 0.23$. The specimen is from a polycarbonate sheet with residual stress due to forming; for the field of view of the specimen, the through-thickness averaged residual stresses are determined to be $\sigma_{xx}^{resid} \approx 1.9$ MPa, $\sigma_{yy}^{resid} \approx -1.9$ MPa, and $\sigma_{xy}^{resid} \approx -0.1$ MPa. Prior to loading, the specimen is imaged using both photoelasticity and CGS; the full-field residual stresses are determined from these measurements. The data field are fairly uniform for the field of view, so the values stated above are assumed to be uniform for the field of view for the theoretical solution. In this example, the specimen is compressed by 23.4 N along the y axis. The derivation of the stress field based on Williams (1952) presented in Section 2.3 is used as the theoretical stress field solution with the addition of the residual stress. For this particular example, the applied stress σ_{app} is -1.84 MPa, and the fitting parameter C_f is 0.76, as determined by comparing the experimental and theoretical in-plane stress fields.

The monochromatic CCD cameras used in this study are IMPERX model IPX-1M48-L with a 1000 × 1000 pixel chip. The optical field of view imaged onto the sensor is 4.0 mm × 4.0 mm, and the image resolution is 4.0 μm. For the CGS setup, the Ronchi grating pitch, p, is 1 mm/40; the grating separation, $\tilde{\Delta}$, is 13.40 mm; the wavelength of light from the linearly polarized HeNe laser

is 632.8 nm; and the resulting lateral shearing distance, d_{shear}, is 339 μm. The first polarizer and $\lambda/4$ plate are set to $\rho = \pi/2$ and $\xi = 3\pi/4$.

3.3.2 Phase Analysis and Stress Determination

3.3.2.1 Image Data

The six experimental phase-shifted photoelastic images are shown in Figure 3.3. The origin is located at the notch tip, acting as the reference to colocate the photoelasticity and CGS images. In this experimental setup, due to small wedge angles in the output $\lambda/4$ plate and polarizer, the rotation of these optics to obtain the six photoelastic images results in very small lateral translations of the images relative to the CCD chip, on the order of 10 or fewer pixels. To mitigate errors due to this translation, the notch tip and other spots, such as small dust particles on the surface of the specimen, are used to colocate the six images. This operation slightly reduces the field of view on the order of 3% or less because only pixels that can be colocated are used, but these lost points are only on the edges of the field of view away from the region of interest. The slight rings in the photoelastic images centered around the notch tip are due to interference of reflections from the front and back faces of the specimen and are a by-product of the coherent monochromatic light source necessary for CGS. These weak interference contours are known as Fizeau fringes and scale in frequency by the thickness variation of the specimen (Hecht, 2002). An anti-reflective coating on the specimen can reduce this effect. Prior to phase analysis, these photoelasticity images are lightly filtered using a Wiener filter, which is a 2D adaptive noise-removal filter design to remove additive noise, of window size $[40 \times 40]$ to reduce these rings.

The experimental photoelastic images may be compared to the theoretical images in Figure 3.4, defined by the stress fields from Equation (2.27), using the experimental σ_{app} and the fitting coefficient, C_f, as described above. Generally, these images compare well with the correct shapes, though the theoretical fields appear to be slightly less dense than the experimental images, as evident in the slightly different locations of the dark fringes in I_1 and I_2. These slight differences are due to two factors: (i) the upper compressive platen is designed to tilt as needed to align with the top of

the plate by sitting against a spherical ball aligned with the center of vertical loading bar, but large angles of misalignment between the specimen and platen led to slightly nonuniform loading of the specimen along the x axis, and (ii) the fitting coefficient C_f is chosen by minimizing error for all the experimental data, not just the photoelastic data, leading in this case to a smaller C_f than indicated by the photoelastic data alone. Also, the experimental and theoretical I_4 and I_6 do not have quite the same behavior near the notch edges, where the theoretical data seems to have poorer fringe contrast than the experimental data. This difference is likely due to a difference in the experimental and theoretical α, which is based on the assumption of uniform residual stresses. The specimen may have some nonuniform residual stresses near the notch edges where the residual stresses may have been relieved due to the cuts for specimen preparation, leading to a different experimental α near the notch edges. Though with less fringe contrast than in the theoretical I_3 and I_5, the dark fringes emanating from the notch tip for $|\theta| > \pi/2$ in the experimental I_3 and I_5 have the correct shape and location. The theoretical photoelastic images do not exhibit the rings centered around the notch tip that are in the experimental images because the Fizeau fringes are not modeled here, showing that these rings are not due to the photoelastic effect, which motivates the Wiener filtering of the experimental images to reduce the effect of these fringes.

Figures 3.5–3.8 show the experimental and theoretical CGS images for the horizontal and vertical shearing directions for the circularly polarized electric field input configuration. The experimental horizontal shearing data in Figure 3.5 compare well with the theoretical data Figure 3.6 in shape, fringe, density, and the interference beading (breaks in the fringe patterns due to superposition of two interference patterns). The experimental vertical shearing data in Figure 3.7 also compare well with the theoretical images in Figure 3.8, though due to the finite shearing distance, the two lobes are slightly further apart than in the theoretical images. The experimental vertical images have the expected interference beading. For both shearing directions, the $\pi/2$ phase shifts between each successive image matches the expected behavior. The finite shearing distance is visible in the doubling of the V-notch boundary. The theoretical images do not include this, but are purely based on the derivatives of $\sigma_1 + \sigma_2$ with a mask for the V-notch that does not model the doubling of the V-

notch. Due to the finite shearing distance, the vertical shearing images in Figure 3.7 cannot capture the lobes on either side of the V-notch boundary prominent in the theoretical data in Figure 3.8.

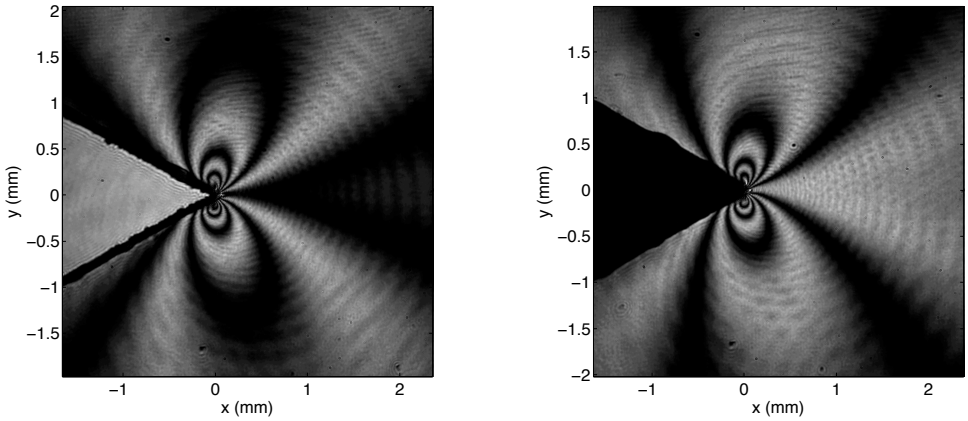

(a) $I_1 = I_o(1 + \cos(\delta))$

(b) $I_2 = I_o(1 - \cos(\delta))$

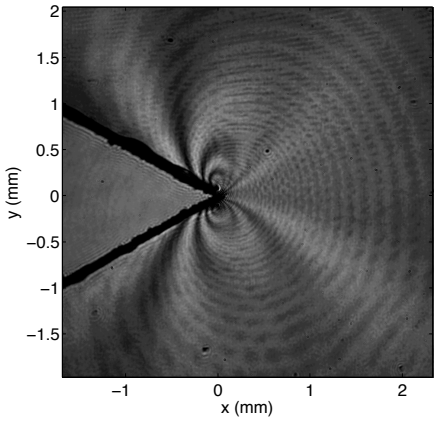

(c) $I_3 = I_o(1 - \sin(\delta)\sin(2\alpha))$

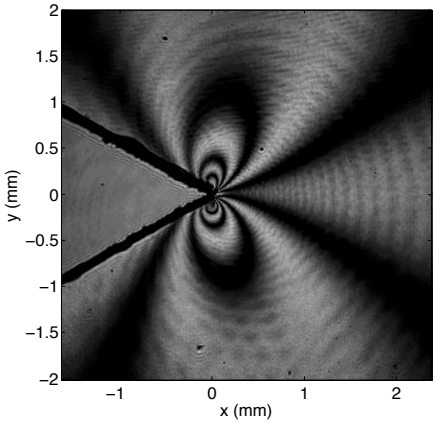

(d) $I_4 = I_o(1 + \sin(\delta)\cos(2\alpha))$

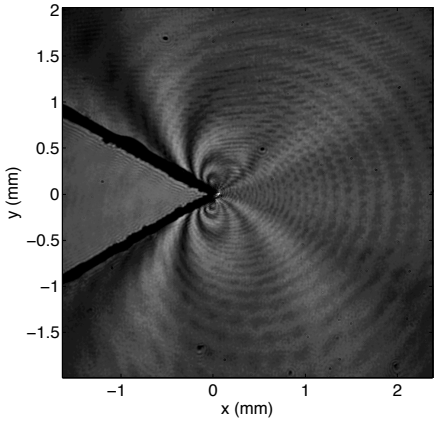

(e) $I_5 = I_o(1 + \sin(\delta)\sin(2\alpha))$

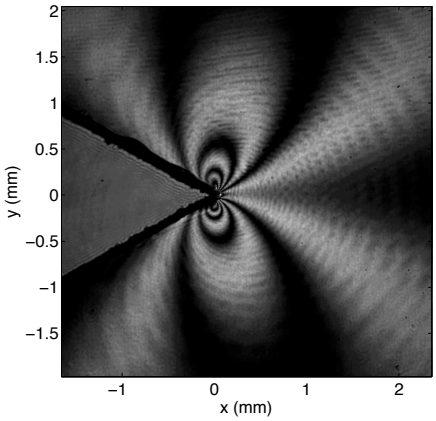

(f) $I_6 = I_o(1 - \sin(\delta)\cos(2\alpha))$

Figure 3.3: Experimental images from six-step phase-shifting photoelasticity for polycarbonate compressed V-notch specimen

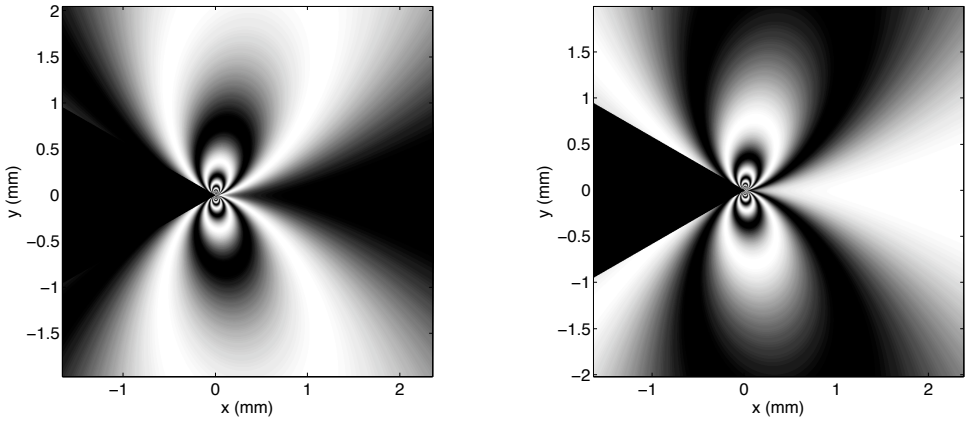

(a) $I_1 = I_o(1 + \cos(\delta))$

(b) $I_2 = I_o(1 - \cos(\delta))$

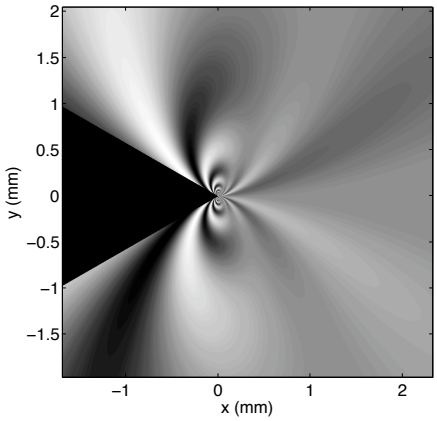

(c) $I_3 = I_o(1 - \sin(\delta)\sin(2\alpha))$

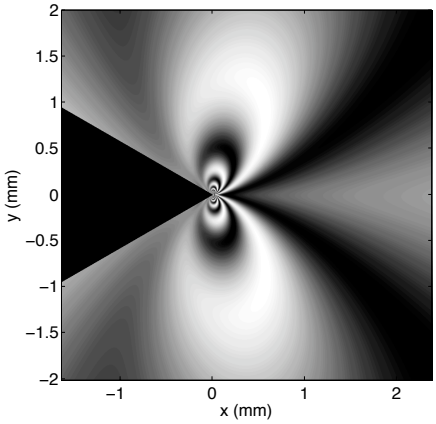

(d) $I_4 = I_o(1 + \sin(\delta)\cos(2\alpha))$

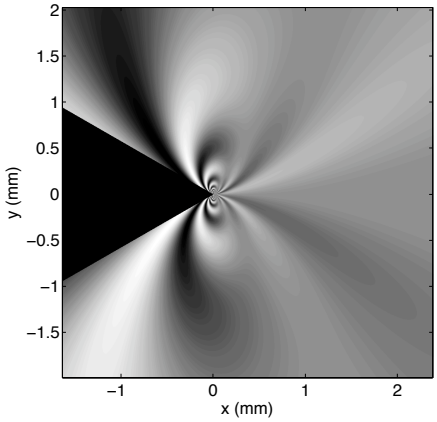

(e) $I_5 = I_o(1 + \sin(\delta)\sin(2\alpha))$

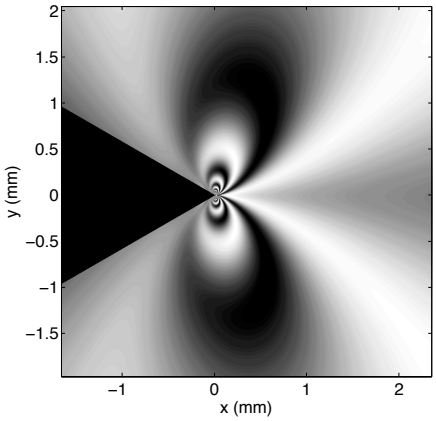

(f) $I_6 = I_o(1 - \sin(\delta)\cos(2\alpha))$

Figure 3.4: Theoretical images from six-step phase-shifting photoelasticity for polycarbonate compressed V-notch specimen

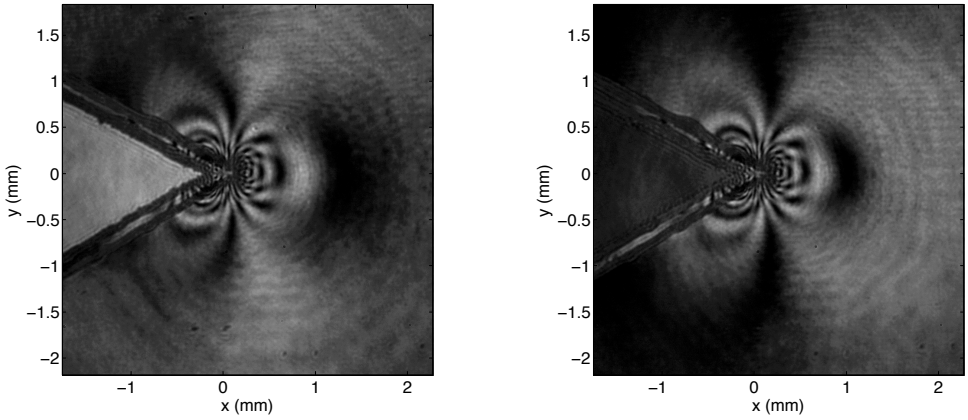

(a) I_1^{circ} (b) I_2^{circ}

(c) I_3^{circ} (d) I_4^{circ}

Figure 3.5: Experimental phase-shifted images from horizontal shearing CGS using the $\lambda/4$ polarization method for compressed polycarbonate V-notch plate

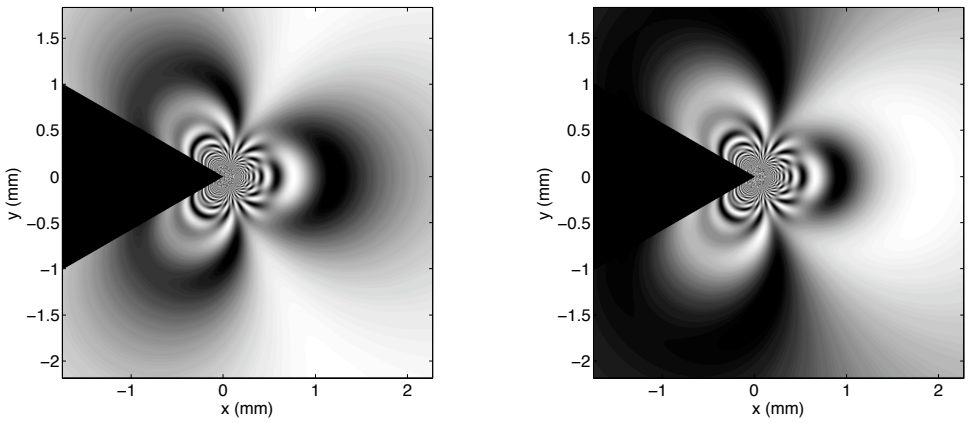

(a) I_1^{circ} (b) I_2^{circ}

(c) I_3^{circ} (d) I_4^{circ}

Figure 3.6: Theoretical phase-shifted images from horizontal shearing CGS using the $\lambda/4$ polarization method for compressed polycarbonate V-notch plate with the notch mask in black

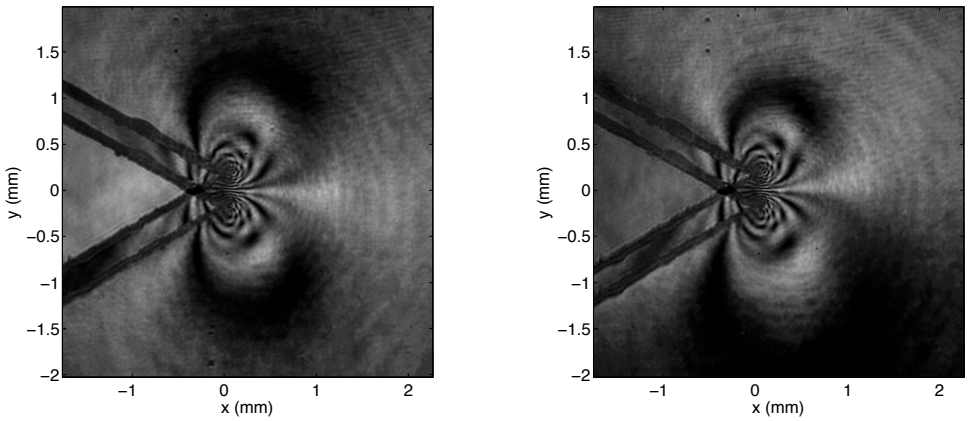

(a) I_1^{circ} (b) I_2^{circ}

(c) I_3^{circ} (d) I_4^{circ}

Figure 3.7: Experimental phase-shifted images from vertical shearing CGS using the $\lambda/4$ polarization method for compressed polycarbonate V-notch plate

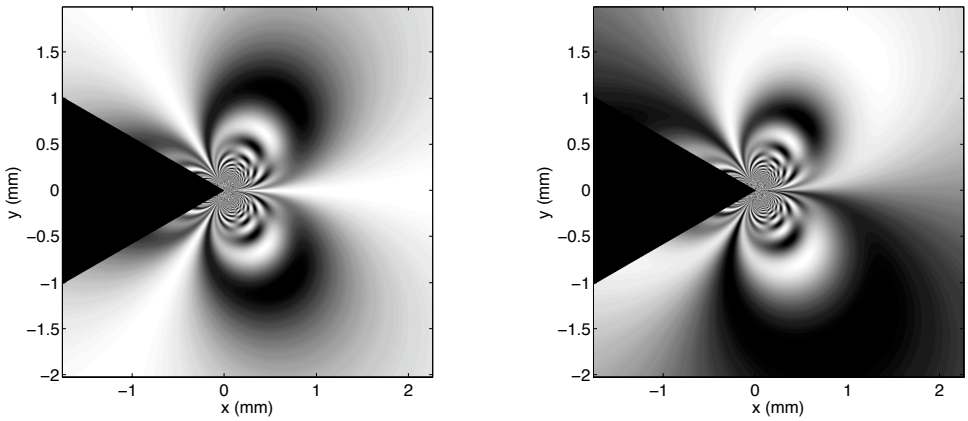

(a) I_1^{circ} (b) I_2^{circ}

(c) I_3^{circ} (d) I_4^{circ}

Figure 3.8: Theoretical phase-shifted images from vertical shearing CGS using the $\lambda/4$ polarization method for compressed polycarbonate V-notch plate with the notch mask in black